PHYSICAL REVIEW B VOLUME 59, NUMBER 8 15 FEBRUARY 1999-II

Electronic and optical properties of strained quantum dots modeled by 8-band k·p theory

O. Stier, M. Grundmann, and D. Bimberg
Institut für Festkörperphysik, Technische Universität Berlin, PN 5-2, Hardenbergstraße 36, D-10623 Berlin, Germany
(Received 10 September 1998)

We present a systematic investigation of the elastic, electronic, and linear optical properties of quantum dot double heterostructures in the frame of eight-band **k·p** theory. Numerical results for the model system of capped pyramid shaped InAs quantum dots in GaAs (001) with {101} facets are presented. Electron and hole levels, dipole transition energies, oscillator strengths, and polarizations for both electron-hole and electron-electron transitions, as well as the exciton ground-state binding energy and the electron ground-state Coulomb charging energy are calculated. The dependence of all these properties on the dot size is investigated for base widths between 10 and 20 nm. Results for two different approaches to model strain, continuum elasticity theory, and the Keatings valence force field model in the linearized version of Kane, are compared to each other. [S0163-1829(99)04608-1]

I. INTRODUCTION

A few years ago the first experimental evidence using temperature dependent cathodoluminescence experiments was obtained for the existence of zero-dimensional (0D) electronic states in self-organized InAs/GaAs quantum dots (QDs) which had been fabricated by Stranski-Krastanow growth during molecular beam epitaxy.[1] Since then this type of QDs has emerged as one of the most extensively studied systems.[2] Today, a large number of experimental results has been reported, addressing the epitaxy, as well as structural, optical and transport properties. QD lasers have been reported which operate at room temperature both c.w. and pulsed up to ≈ 10 GHz.[3,4]

The size and shape of Stranski-Krastanow grown InAs QDs on GaAs (001) reported by different authors vary, dependent on the epitaxial method and particularly on the growth conditions used: Pronounced pyramidal shape or a less pointed dome shape, side facets oriented along {101},[5] {105},[6] {113},[7] {114},[8,9] {136},[10] and different sizes of QDs have been reported.

Similarly, low temperature spectra of a few or single QDs exhibit a rich excitonic fine structure, but differ according to the growth conditions.[11–14] For larger ensembles of QDs inhomogeneous line broadening of presently $\geqslant 30$ meV (Ref. 1) due to fluctuations of size, shape, and chemical composition disguises some of this fine structure. Nevertheless, transitions due to higher energy electronic states are clearly visible in calorimetric absorption, and photoluminescence excitation spectra.[1] Unambiguous assignment of these fundamental transitions is still pending. In order to obtain meaningful interpretations, advanced numerical bandstructure calculations must be correlated with precise information about the structural properties of the QDs.

Large effort has been expended at the theoretical modeling of QD systems. From the beginning it was clear that the lattice-mismatch-induced strain in the QD has a dominant influence on the energy level structure.[15,16] Early works treated the strain within the continuum mechanical theory (CM) either analytically[15] or numerically by the finite differences method.[16] The QD shape was assumed in Ref. 16 to be a pyramid with {101} side facets, in agreement with results in Ref. 5. The band structure was calculated in the frame of an effective mass approximation with parabolic bands. For some time, the finding that there is at most one bound electron state in this QD type for pyramid base lengths $b \leqslant 18$ nm was not contraverted and led to the interpretation of multiple spectral lines as a fingerprint of the valence band (VB) spectrum.

More recently, the conduction band (CB) reentered the focus of interest, stimulated by capacitance,[17] photoluminescence,[18] and excitation spectroscopy[19] results pointing to the existence of several excited electron levels in InAs/GaAs dots for $b \leqslant 20$ nm. Consequently, theorists revisited the problem of electron states in such QDs, now using different effective masses,[20] perturbational effective mass approaches,[21] eight-band **k·p** theory,[22–25] and empirical pseudopotential theory.[26] All approaches now yield generate several electron states for $b \geqslant 10$ nm, however, varying predictions for both the number and actual energies of the levels were obtained in successive works of the same authors and in comparison of works of different authors. E.g., in Ref. 24 at most four electron levels were reported for $b \leqslant 18$ nm while we reported six for $b = 17$ nm.[25] Some of the persisting discrepancies might be explained by the fact that some authors[21–23] do not take into account piezoelectric effects, despite of their important influence on the optical properties which was demonstrated already in earlier work,[16] and which is emphasized here.

In this paper we present a systematic investigation of the size dependence of the electronic and linear optical properties of capped single InAs pyramid QDs with {101} facets on GaAs (001) as a model system. We consider the size range $10\,\mathrm{nm} \leqslant b \leqslant 20\,\mathrm{nm}$ and calculate the single electron and hole states on the basis of eight-band **k·p** theory. The influence of the input material parameters on the resulting energies is discussed.

Since the impact of strain on the carrier confinement is comparable to that of the band offset due to the variation of the chemical composition at the heterojunctions, the wave functions and energies are very sensitive to the underlying strain distribution. We analyze for the first time the influence

 ©1999 The American Physical Society

of different strain models on the energy levels: The CM model using the known compliances C_{11}, C_{12}, C_{44} is compared to the linearized valence force field (VFF) model and to a CM calculation employing the ''incorrect'' value of C_{44} implicitly assumed in the VFF model. The piezoelectric effect is treated including the image charge effects at the heterojunctions.

The ground-state exciton binding energy and the electron Coulomb charging energy are calculated within the Hartree approximation, accounting for image charge effects. Finally, we calculate the polarization dependent oscillator strength of optical transitions between electrons and holes, and between electrons, again for the two strain models, and accounting for the spatial, **k**, and strain dependence of the momentum operator.[27] In particular we find transitions between electronic levels whose oscillator strengths reach up to 20% of the electron-hole ones. All transitions exhibit pronounced polarization anisotropy. We present linear absorption spectra for both types of transitions.

II. CALCULATION OF STRAIN

A. Continuum mechanical model (CM)

The total strain energy in the continuum mechanical model is given by[28]

$$U_{\mathrm{CM}}=\frac{1}{2}\sum_{i,j,k,l} C_{ijkl}\epsilon_{ij}\epsilon_{kl}. \tag{1}$$

For a given structure it is minimized, using finite differences for the strains $\epsilon_{ij}=\partial u_i/\partial x_j$, where $\mathbf{u}$ is the displacement vector field. The compliances C_{ijkl} are represented by the parameters C_{11}, C_{12}, and C_{44} for cubic crystals. The strain distribution in capped InAs pyramids on a thin InAs wetting layer in GaAs has been calculated in a finite differences scheme by us previously.[16] A conjugate gradient method is employed at 2×10^6 voxels for the numerical calculation. At interfaces, the condition of a continuous stress tensor yields the proper boundary conditions. In order to avoid oscillatory solutions arising when symmetric difference quotients are used, the energies from the eight possible combinations of forward and backward differences in the three directions are averaged as in Ref. 16.

B. Valence force field model (VFF)

Sufficiently small QDs can also be directly modeled with the VFF model.[29–32] The elastic energy of each atom is written in terms of the positions of its nearest neighbor atoms and then added up for all atoms. In the version of Keating,[30] the elastic energy U_{VFF} of the crystal is written as a sum over all atoms i and given as

$$U_{\mathrm{VFF}}=U_\alpha+U_\beta, \tag{2}$$

$$U_\alpha=\frac{1}{4}\sum_i\left[\frac{\alpha_{ij}}{4}\sum_j\frac{(\mathbf{r}_{ij}\cdot\mathbf{r}_{ij}-3d_{ij}^2)^2}{d_{ij}^2}\right], \tag{3}$$

$$U_\beta=\frac{1}{4}\sum_i\left[\sum_j\sum_{k\neq j}\frac{\beta_{ijk}(\mathbf{r}_{ij}\cdot\mathbf{r}_{ik}+3d_{ij}d_{ik})^2}{2d_{ij}d_{ik}}\right], \tag{4}$$

TABLE I. Ratio κ according to Eq. (8) for different semiconductors.

	Si	Ge	GaAs	InAs	InP
κ	0.99	1.07	1.13	1.22	1.20

where the sums over j and k run over the four tetrahedrally coordinated nearest neighbor atoms, $\mathbf{r}_{ij}$ denotes the vector from the ith atom towards its jth neighbor, and $4d_{ij}$ is the lattice constant of the binary (or elementary) $i-j$ constituent. U_α in Eq. (2) is nonzero when the bond *length* is changed from the strain-free state and is thus called the ''bond-stretching'' interaction. U_β in Eq. (2) is nonzero when the *angle* between bonds is altered and is thus called ''bond-bending'' interaction.

By comparison with the cubic strain tensor it follows that α and β can be expressed in terms of C_{11} and C_{12}:[30]

$$\alpha=(C_{11}+3C_{12})d, \tag{5}$$

$$\beta=(C_{11}-C_{12})d. \tag{6}$$

In a ternary compound or across a heterointerface the β parameter is geometrically averaged if the atoms j and k are not identical: $\beta_{ijk}=\sqrt{\beta_{ij}\beta_{ik}}$.[33] Since this VFF model works with two parameters only, C_{44} is no independent elastic modulus anymore but fixed to the value

$$C_{44}=\frac{\alpha\beta}{(\alpha+\beta)d}, \tag{7}$$

i.e.,

$$\kappa=\frac{2C_{44}(C_{11}+C_{12})}{(C_{11}-C_{12})(C_{11}+3C_{12})}\equiv 1. \tag{8}$$

This relation is fulfilled for silicon. For a number of other important semiconductors there are deviations up to 22% (InAs), see Table I.

The potential of Eq. (2) is not harmonic, and other authors[34] used this unharmonic Keating model for calculations of the strain distribution in InAs/GaAs QDs. However, as remarked by Kane,[32] anharmonic effects due to the higher order terms have not been shown to be satisfactorily treated by the Keating model. In particular, the third-order elastic moduli C_{ijk} (Ref. 35) do not enter the theory. Therefore we will use in the following a linearized version of U_α and U_β in Eq. (2) as proposed in Ref. 32.

We note that in addition second-nearest-neighbor bond-stretching, contiguous bond bending and the so-called MSBN interaction[36] can be included. The eight parameters of Solbrigs model[36] have to be determined from fits to experimental phonon dispersion curves. It has been applied to InAs/GaAs pyramids[20] but we do not pursue this approach here in order to avoid its excessive numerical expense. Instead, two easily tractable models, CM and the linearized Keating model, are compared. The strain distribution in a InAs/GaAs QD with $b=13.6$ nm as obtained from the CM model is shown in Fig. 1.

The differences between the strain distributions in a pyramid calculated within the CM and the (linearized) VFF mod-

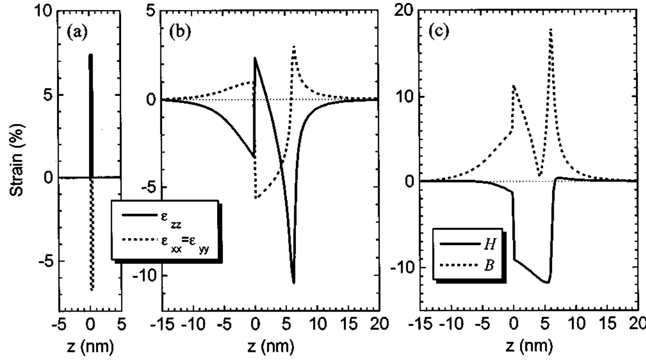

FIG. 1. Strain distribution in and around an InAs pyramid ($b = 13.6$ nm) bounded by {101} facets on a one monolayer (ML) thick InAs wetting layer (WL) within a GaAs matrix, according to the continuum mechanical (CM) model, and along [001] line scans: (a) through the WL far away from the dot, (b) and (c) through the pyramid tip. (a) and (b) show the diagonal elements of the strain tensor and (c) depicts the hydrostatic (H) and biaxial (B) strain components: $H=\epsilon_{xx}+\epsilon_{yy}+\epsilon_{zz}$, $B^2=(\epsilon_{xx}-\epsilon_{yy})^2+(\epsilon_{yy}-\epsilon_{zz})^2+(\epsilon_{zz}-\epsilon_{xx})^2$.

els are shown in Fig. 2. Two different continuum mechanical models are compared: first the CM with the correct value of C_{44}, and second the CM[C_{44}^{VFF}] where C_{44} takes the incorrect value implied by the two-parameter Keating model according to Eq. (7). The main differences between the VFF and CM models are the following:

(1) At the tip of the pyramid the diagonal strain components ϵ_{ii} analytically diverge in continuum theory while the VFF model yields a finite value. A numerical solution of the CM model using finite differences with a voxel size of one atom yields a similar value, however.

(2) At interfaces the VFF and CM models differ on the atoms directly adjacent to the interface.

(3) In the volume, differences between VFF and CM are mainly due to the incorrect value of C_{44} in VFF. They almost disappear if VFF is compared to CM[C_{44}^{VFF}], which uses the incorrect C_{44} value according to Eq. (7).

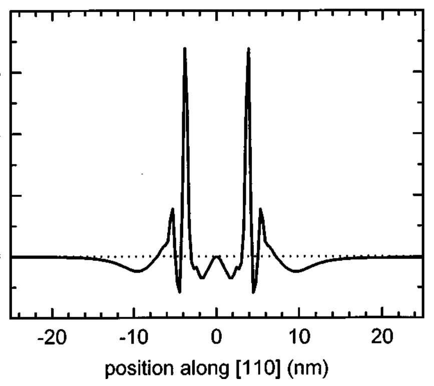

FIG. 3. Difference of ϵ_{zz} along the [110] and [$1\bar{1}0$] directions along a [110] line scan through the center of an InAs pyramid ($b = 13.6$ nm) on a 1-ML-thick WL, calculated within the VFF model.

(4) The symmetry of the CM strain tensor in the (001) plane is C_{4v}. The tetrahedral configuration of atoms in the VFF model leads to a C_{2v} symmetry, i.e., strain components are different along the [110] and [$1\bar{1}0$] directions, as already noted in Ref. 34. This is visualized in Fig. 3, where the difference of the strain component ϵ_{zz} along the [110] and [$1\bar{1}0$] directions is plotted. In the CM model (for any value for C_{44}) this difference is *a priori* zero.

The influence of these differences on the energy levels and wave functions of charge carriers in the QD will be discussed below.

III. PIEZOELECTRICITY

Regardless of the chosen strain model, the symmetry of the carrier confinement is only C_{2v} due to piezoelectric charging of the QD. From the strain tensor (ϵ_{ij}) and the piezoelectric modulus e_{14} the piezoelectric charge density

$$\rho_p(\mathbf{r})=\mathrm{div}[e_{14}(\mathbf{r})\cdot\{\epsilon_{yz}+\epsilon_{zy},\epsilon_{xz}+\epsilon_{zx},\epsilon_{xy}+\epsilon_{yx}\}(\mathbf{r})] \tag{9}$$

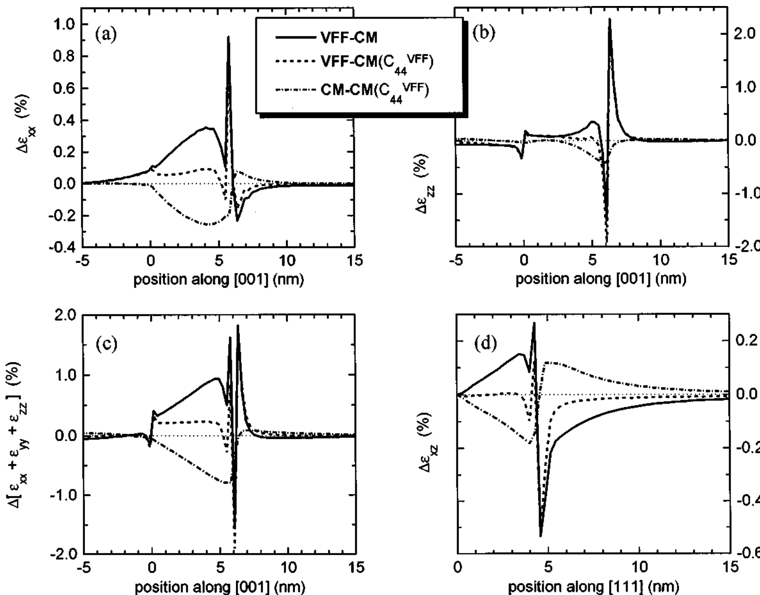

FIG. 2. Strain distributions in an InAs pyramid ($b = 13.6$ nm) on a 1-ML-thick WL. The differences between the (linearized) valence force field (VFF) model, CM, and CM with the value for C_{44} according to Eq. (7) used in VFF (CM[C_{44}^{VFF}]) are compared. (a) ϵ_{xx}, (b) ϵ_{zz}, (c) hydrostatic strain along [001] through the center of the pyramid, (d) shear component ϵ_{xz} along [111], originating at the bottom center of the pyramid. Solid (dashed) lines represent the difference between the VFF and CM (CM[C_{44}^{VFF}]) models. Dash-dotted lines show the difference between the CM and CM[C_{44}^{VFF}] models.

is calculated. Equation (9) introduces C_{2v} symmetry to the Hamiltonian Eq. (12) even when (ϵ_{ij}) possesses C_{4v} symmetry: The polarization charges mainly form dipoles along the edges of the pyramid, see Ref. 16, and the polarities of the dipoles alter between inside and outside the QD as well as between neighboring edges. At edges along $[1\bar{1}1]$ and $[1\bar{1}\bar{1}]$, the negative charges are located inside the QD. This implies that the $[1\bar{1}0]$ direction will be the favorable direction for the extension of hole wave functions, while electrons will prefer to expand along $[110]$.

The associated Coulomb potential $V_p(\mathbf{r})$ is obtained from the Poisson equation Eq. (10),

$$\rho_p(\mathbf{r}) = \epsilon_0 \nabla [\epsilon_s(\mathbf{r}) \nabla V_p(\mathbf{r})], \tag{10}$$

$$\Leftrightarrow \Delta V_p(\mathbf{r}) = \frac{\rho_p(\mathbf{r})}{\epsilon_0 \epsilon_s(\mathbf{r})} - \frac{1}{\epsilon_s(\mathbf{r})} \nabla V_p(\mathbf{r}) \cdot \nabla \epsilon_s(\mathbf{r}), \tag{11}$$

where $\epsilon_s(\mathbf{r})$ is the static dielectric constant of the respective material at position $\mathbf{r}$.[37] The first term on the right-hand side of Eq. (11) refers to the true three-dimensional charge density while the second is the contribution of polarization surface charge densities due to discontinuous dielectric constants at heterointerfaces (the singularity of $\nabla \epsilon_s$ is integrable), usually discussed as image charges.[38–40] Numerically, Eq. (10) needs to be solved on a substantially larger space region than the band structure equation Eq. (12), and using Dirichlet boundary conditions. Otherwise a too small spatial modulation of $V_p(\mathbf{r})$ may be obtained.

The piezoelectric potential $V_p(\mathbf{r})$ essentially scales proportionally to the QD size, and for larger dots its influence on bound particle states dominates over that of immediate C_{2v} symmetry effects from the VFF strain distribution.

IV. EIGHT-BAND k·p MODEL FOR QUANTUM DOTS

The energy levels and wave functions of bound electron and hole states are calculated in the frame of the eight-band $\mathbf{k}\cdot\mathbf{p}$ model. This model was originally developed for and succesfully applied to the description of electronic states in bulk materials[27,41–43] and quantum wells.[44] Recently it has been implemented for numerical calculations of electronic properties of quantum wires[45] and QDs.[22–25] For details of the principles of our implementation see Ref. 45. We use the spatial representation of the Hamiltonian H and obtain a system

$$H(x,y,z,\partial_x,\partial_y,\partial_z,\partial_{xx},\partial_{xy},\partial_{xz},\partial_{yy},\partial_{yz},\partial_{zz})\Psi(x,y,z) = E\Psi(x,y,z) \tag{12}$$

of eight coupled partial differential equations for the eight complex envelope functions

$$\Psi = (\psi_{s\uparrow},\psi_{x\uparrow},\psi_{y\uparrow},\psi_{z\uparrow},\psi_{s\downarrow},\psi_{x\downarrow},\psi_{y\downarrow},\psi_{z\downarrow}). \tag{13}$$

Our model allows us to treat QDs of arbitrary shape and material composition, including the effects of strain, piezoelectricity, VB mixing, and CB-VB interaction. So far strain gradient terms $\nabla_{\mathbf{r}}(\epsilon_{ij})$ (Ref. 46) and the strain dependence of the spin-orbit interaction[47] have been neglected. Those eigensolutions (E_n,Ψ_n) of Eq. (12) that vanish on the boundary ∂G of the calculation region G, i.e., the integrable ones, are the bound states of charge carriers in the QD. We use the finite differences method we have proposed in Ref. 45 except that the Dirichlet condition $\psi|_{\partial G} \equiv 0$ is not enforced, because it either disturbs the convergence of the eigensolver or, otherwise, is (for bound states) fulfilled anyway. Like for the local pseudopotential method the computational expense is not causally related to the number of atoms in the structure (the grid spacing can be chosen independently, and can be scaled), so that in this respect it deserves the predicate "sublinear,"[48] and it still can be executed on single workstations (433 MHz DEC α in our case).

The treatment of the thin wetting layer (WL) is difficult because its thickness usually is represented by a too small number of voxels. The problem is circumvented by modeling the WL as quantum well with graded composition, reproducing the integral indium amount. Two-dimensional (2D) states confined in the WL but not in the QD appear at higher energies and indicate the end of the zero-dimensional (0D) spectrum. The effort expended at modeling the WL only aims to obtain the transition from 0D to 2D states at plausible energies. The bound states obtained from our method are accurate apart from the discretization error (discussed below), but the numerical 2D-like states are not realistic and therefore not included in this paper.

The material parameters we have used are summarized in Table II. We find no numerical requirement[45,52] that the Kane parameters satisfy $A'>0$, $L'<0$, $M<0$, and $N'<0$ (see Refs. 41,44 for their definition, we note that A' in Ref. 44 is equal to $A'+\hbar^2/2m_0$ in Ref. 41). The $\mathbf{k}\cdot\mathbf{p}$ model, when applied to small quantum structures, has in principle a few well-known general drawbacks which have been examined in detail.[48,56] The drawbacks are related to the conceptionally fixed number of Bloch functions (eight in our case) used for expanding the wave functions, the restriction to the Brillouin zone center Γ, the assumption of the same Bloch functions throughout the entire structure (regardless of material and strain variations), the arbitrariness of the matching conditions for the envelopes at heterointerfaces (leading to heuristic secular equations for the eigenvalues). These problems do not arise in microscopic theories like semiempirical pseudopotential theory[48] (to our knowledge no modeling of capped QDs by the tight-binding model was reported), which potentially have some greater accuracy. However, at present this potential can hardly be exhausted since a large accuracy of output requires a large accuracy of input. As will be shown below, the results of pseudopotential calculations[48] are qualitatively very similar to those obtained by eight-band $\mathbf{k}\cdot\mathbf{p}$ theory, although they differ substantially from those of one-band effective mass theory. The variance in the numerical data on some material properties makes the advantages of microscopic theories over envelope function theory look unsubstantial for the moment. Most important, the eight-band $\mathbf{k}\cdot\mathbf{p}$ method requires much less computational resources.

V. BOUND SINGLE PARTICLE STATES

We calculate the electron and hole level energies and wave function probability densities for four different QD sizes (base widths b: 10.2 nm, 13.6 nm, 17.0 nm, 20.4 nm) and two strain models (CM and VFF). We assume the same

TABLE II. Material parameters for 6.5 K used in this work.

Quantity		Unit	Value for $In_cGa_{1-c}As$	Reference
Lattice constant	a	Å	$5.6503+0.4050c$	49
Fundamental gap	E_0	meV	$1518-1580c+475c^2$	49
Averaged VB edge[50]	E_v'	meV	$-6920+231c-58c^2$	45,49
Spin-orbit coupling energy	Δ_0	meV	$340-93c+133c^2$	51
Optical matrix parameter	E_p	meV	$(1.238-0.2095c)\frac{1-m_e}{m_e}\frac{3E_0(E_0+\Delta_0)}{3E_0+2\Delta_0}$	52,53
CB effective mass	m_e	m_0	$0.0667-0.0419c-0.00254c^2$	54
Luttinger parameter	γ_1		$1/[(1-c)/7.10+c/19.7]$	51,55
Luttinger parameter	γ_2		$1/[(1-c)/2.02+c/8.4]$	51,55
Luttinger parameter	γ_3		$1/[(1-c)/2.91+c/9.3]$	51,55
Kane parameter	B	meV nm^2	0	44,45
CB-VB coupling by strain	b'	meV	0	44,45
CB hydrostatic def. pot.	a_c	meV	$-8013+2933c$	54
gap hydrostatic def. pot.	a_g	meV	$-8233+2153c$	54
VB shear def. pot. [100]	b_v	meV	$-1824+24c$	51
VB shear def. pot. [111]	d_v	meV	$-5062+1462c$	51
Elastic compliance	C_{11}	GPa	$118.8-35.5c$	51,55
Elastic compliance	C_{12}	GPa	$53.8-8.5c$	51,55
Elastic compliance	C_{44}	GPa	$59.4-19.8c$	51,55
Static dielectric constant		ϵ_s	$13.18+1.42c$	54
Piezoelectric modulus	e_{14}	C m^{-2}	$0.160-0.115c$	54

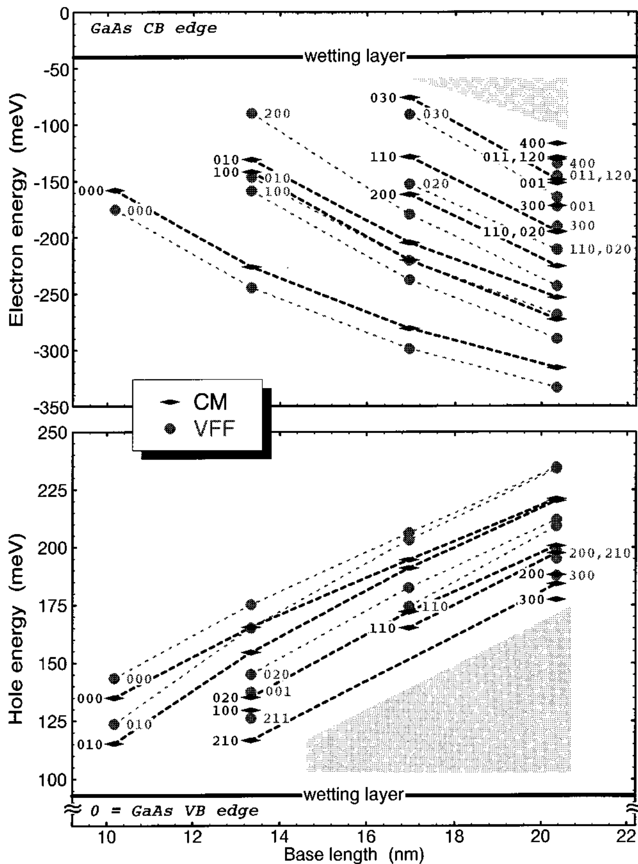

FIG. 4. Electron and hole energies in pyramidal InAs/GaAs QDs for different sizes, calculated using two different linear strain models. The dashed lines connect levels having the same wave function symmetry, labeled by the appropriate ''quantum numbers'' (see text for their explanation). Energy levels in the shaded regions are omitted.

InAs/GaAs band alignment as used by us in Ref. 45 where the offset in the unstrained bulk VB Γ_8 is 186 meV (referred to as lineup ''A,'' $\Delta E_c/\Delta E_g=0.83$). This offset differs from the one previously used by us in Ref. 16.

A. Results for strain according to the CM model

Figure 4 shows the energy levels for the strain distributions obtained by the CM model (black diamonds). The WL ground-state levels shown here are taken from Ref. 16, in agreement with experimentally observed transition energies, and are assumed to be independent from the QD size. The ''quantum numbers'' are based on a depictive terminology to graphically describe the shape of the probability density, and refer to the tangential planes of the probability-density nodal surfaces in the order $[110],[1\bar{1}0],[001]$ (see Fig. 5). We emphasize that these are not true quantum numbers: Nodal surfaces exist at most for single envelopes and usually have different orientations for the p-type envelopes $|x\rangle$, $|y\rangle$, and $|z\rangle$ (see Fig. 6). The probability density distributions obtained by (weighted) summation over all envelope contributions have no nodal surface anymore, hence the states possess no well-defined parity.

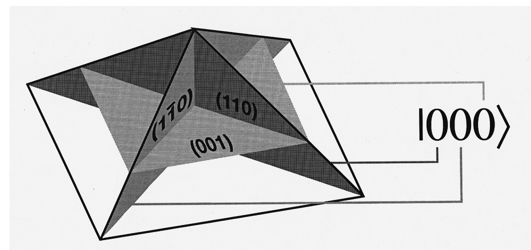

FIG. 5. Tangential planes of the probability-density nodal surfaces used to label bound states.

Electron Ground State

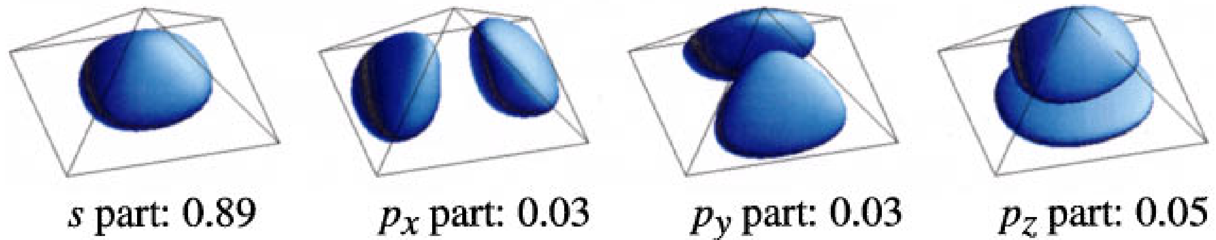

Hole Ground State

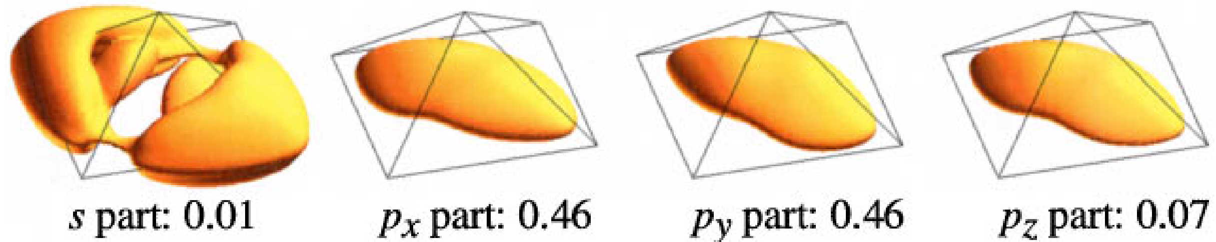

FIG. 6. (Color.) Decomposition of the ground-state wave functions into their constituing single envelopes ($b=13.6$ nm). The numbers denote the integral probability of the respective envelopes after summation over both spins. The electron ground state is mainly represented by *s*-type Bloch functions while the hole ground state is almost completely described by *p*-type Bloch functions.

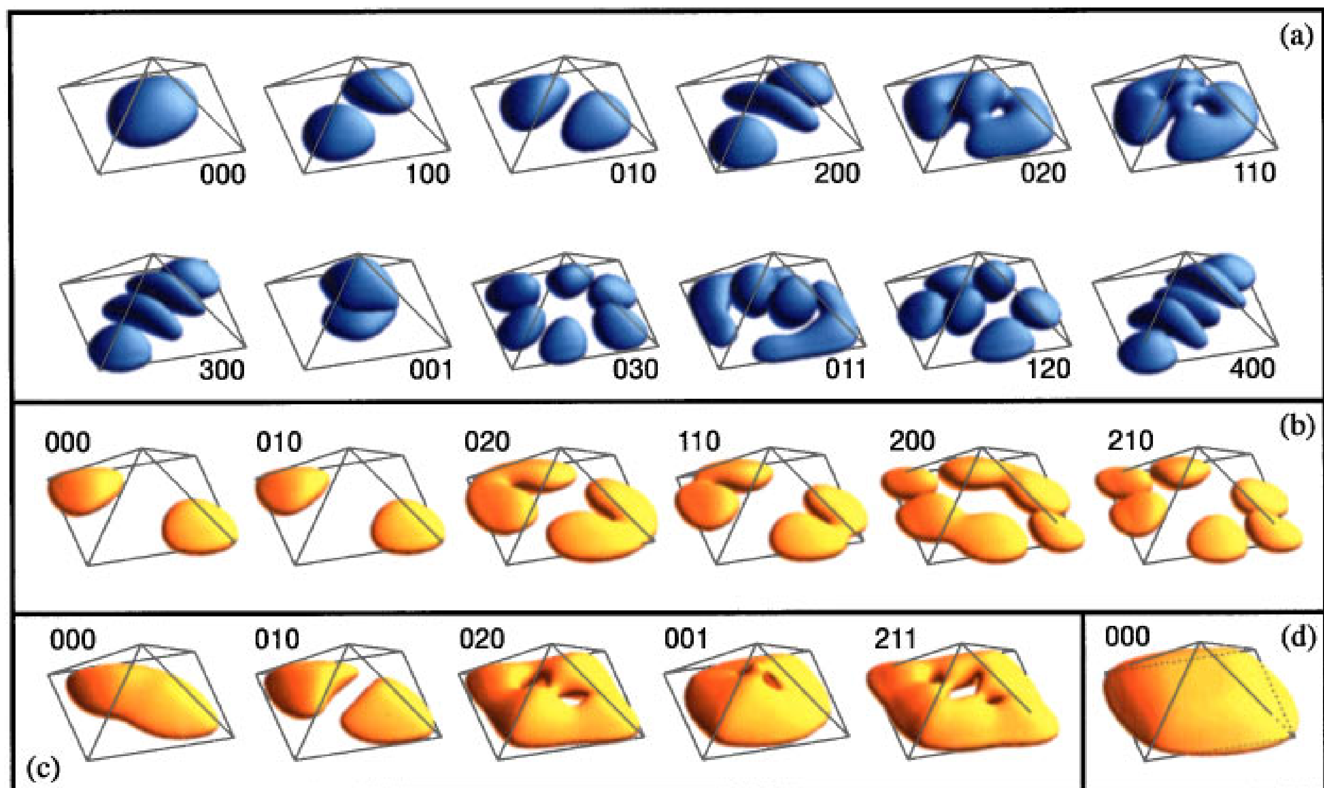

FIG. 7. (Color.) Probability density isosurfaces ($p=65\%$) of (a) the electron and (b) the hole states for $b=20.4$ nm, the strain calculated using the CM model. (c) Hole states for $b=13.6$ nm and strain calculated using the VFF model. The large shape differences between (b) and (c) are mainly due to the different dot sizes and not due to the strain modeling. (d) Hole ground state for $b=13.6$ nm from an effective mass calculation using the same strain distribution as in (c). The ''quantum numbers'' graphically describe the wave-function shapes and originally count the nodal surfaces tangential to (110), $(1\bar{1}0)$, and (001), respectively (see text and Fig. 5).

Due to the piezoelectric field the main directions of extension of the wave functions are [110] for electrons [see Fig. 7(a)] and $[1\bar{1}0]$ for holes [see Figs. 7(b) and 7(c)], while $[ij1]$ only occurs in high energy states in large QDs [see electron state $|001\rangle$ in Fig. 7(a)].

1. Electron levels (CM)

For QDs with $b \leqslant 10$ nm we find at most one bound electron state while for $b=20$ nm there are as many as 12. The prediction of (several) excited electron states in QDs with $b>13$ nm is the most important—though not the only—improvement over previous effective mass calculations.[16] The ground state is always *s*-like (see also Fig. 6), and its shape is slighty elongated along [110]. The first and second excited, *p*-like, states $|100\rangle$ and $|010\rangle$ form a nondegenerate pair, the energy separation between them is approximately proportional to b, in agreement with the proportionality between the piezoelectric potential and b (see above). The separation between the average energy of the *p*-like states and the *s*-like state decreases as the dot size increases. We find no intermixing with WL states, i.e., bound electron wave functions do not extend into the WL.

In Ref. 24 the size dependence of the electron states was also investigated using the CM model and eight-band $\mathbf{k}\cdot\mathbf{p}$ theory, however, finding at most four levels for each size. The reported separations between the average *p*-state energy and the *s*-state or the third excited state agree well with Fig. 4, while the separation between the *p* states is much less than here. In Ref. 21 electron levels were calculated using CM and strain dependent effective masses but neglecting shear strain. These results differ significantly from ours: We find a different sequence of the wave functions and different level separations.

2. Hole levels (CM)

The holes are generally confined to the bottom of the pyramid and do not reach the tip, see Figs. 7(b) and 7(c). Their shapes depend strongly on the QD size, as can be seen by comparing Fig. 7(b) ($b=20.4$ nm) and Fig. 7(c) ($b=13.6$ nm, the VFF-based wave functions shown here to facilitate the comparison with a number of works by other authors look very similar to the CM-based ones). The wave functions of excited hole states extend somewhat into the WL. In contrast to an effective mass calculation using the same strain distribution [see Fig. 7(d)] the ground-state wave functions are pronouncedly elongated along $[1\bar{1}0]$ [see Fig. 7(c)], and also the excited states in the present approach are very different from previous effective mass results[16] with respect to both the wave-function shapes and the level separations. In agreement with Ref. 16, in large QDs the ground-state wave functions are asymptotically torn into two [see Fig. 7(b)], becoming almost degenerate with the first excited level (see Fig. 4, symmetry breaking).

In Fig. 4 higher excited hole levels for $b>16$ nm are omitted. The dependence of the ground-state energy on the dot size is weaker than for electrons, due to the ''larger mass''. The energetic splitting between the first and second excited states ($|010\rangle$ and $|020\rangle$) is comparable to that of the electrons ($|100\rangle$ and $|010\rangle$) but not strictly proportional to b anymore, and both states are not *p*-like either. This emphasizes that 0D holes behave less classically than electrons because of their greater sensitivity to quantum confinement.

In Ref. 24 the first excited hole level shows a different dependence on the dot size. The tendency towards asymptotical degeneracy with the ground state is much weaker while the energy separation between the first and second excited states for $b \geqslant 10$ nm is considerably size dependent. The latter, more classical behavior is surprising in view of the stronger localization reported.

B. Impact of input values

Comparison of results based on different theoretical approaches is hindered by the fact that additionally the material parameters used as input to the calculations partly differ. In order to compare our following results obtained from the VFF model with those of other authors we therefore examine first the influence of variations of the input parameters like the InAs/GaAs band offsets and numerical procedures on the calculated energy levels. Table IV shows some results.

1. Discretization error

The material parameters from Table II are used in sets 1 and 2 of Table IV. In set 2 the finite differences voxel size is the lattice constant, as throughout this work. Set 1 is calculated on a twice as fine grid (8 times more voxels). By comparing the two, the discretization error of the level energies can be estimated to be $\leqslant 10$ meV. Since electron and hole energies shift in the same direction, the error in transition energies is much less.

2. Different material parameters

Set 7 is very similar to the input data from Ref. 23, and sets 3–6 show the transition from set 2 to set 7 (subsequent sets include the changes of previous ones). In set 3 the piezoelectricity is turned off. In set 4 the band alignment is changed: The alignment A used in the present work is based on (still somewhat unsatisfactory) experimental evidence.[49] Another frequently assumed alignment was calculated in Ref. 50 (we call it lineup ''B'') where the Γ_8 offset is 264 meV ($\Delta E_c/\Delta E_g=0.76$). In sets 5 and 6 the optical matrix parameter and the deformation potentials are changed, respectively, and set 7 approximately accounts for the different strain distribution found in Refs. 20 and 23.

The resulting ground-state energy levels are plotted in Fig. 8. The piezoelectricity has little influence on the ground-states energies, but this must not distract from its importance for the excited states wave functions and the related optical properties like oscillator strengths and anisotropies, as discussed below. The band alignment has little influence on the transition energy. The scaling of strain has little influence on the hole ground-state energy, because $|a_v| \ll |a_c|$ for InAs. For smaller optical matrix parameters E_p the transition energy increases which is mainly due to the related effective decrease of the bulk conduction band mass, the holes are much less affected (see Fig. 8).

3. InAs/GaAs band offsets

Obviously, the most important parameter for the energy level positions of electrons and holes with respect to the

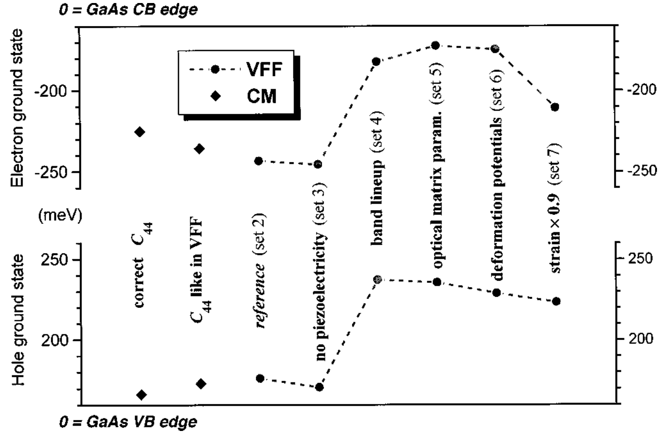

FIG. 8. Ground-state energies for $b=13.6$ nm and different strain models and material parameters which are listed in Tables III and IV. The dotted lines are guides to the eye.

GaAs barrier is the heterojunction band lineup. Unfortunately, this is also the least accurately known parameter. In the case that lineup B were closer to reality than lineup A, in QDs with $b \geqslant 13$ nm the electron ground-state energies would shift upwards by ≈ 70 meV, but the increase of kinetic energy of the holes is approximately equal to the decrease of that of the electrons. Thus the ground-state transition energies would increase by less than 15 meV. Some bound electron states would disappear for large dots as compared to the results of Fig. 4, and some new bound hole states would appear. The relation between the localization energies of the electron and hole ground states would become almost inverted (see Fig. 8).

TABLE III. Ground-state energies (meV) of electrons and holes and the transition energy in an InAs pyramid ($b=13.6$ nm) calculated for three different strain models.

	CM	CM[C_{44}^{VFF}]	VFF
E_{000}^{e}	1292.9	1282.4	1274.5
E_{000}^{h}	166.5	173.1	176.2
ΔE	1126.4	1109.2	1098.4

C. Results for strain according to the VFF model

Figure 4 also shows the energy levels for the strain distributions obtained by the VFF model (gray disks).

1. Difference between CM and VFF

Table III shows the ground-state energies of electrons and holes and the transition energies for the cases that the strain distribution is calculated using CM, VFF, and CM[C_{44}^{VFF}]. The differences between CM[C_{44}^{VFF}] and CM are significantly larger than between CM[C_{44}^{VFF}] and VFF, indicating that the major part of the difference between CM and VFF is due to the incorrect value of C_{44} in the VFF model and not due to its atomistic character. We therefore conclude that the CM model gives a description closer to reality than the (linearized) VFF model. This holds the better the larger the QDs are.

2. Electron levels (VFF)

The electron levels are almost rigidly shifted by -17 meV as compared to the CM calculation. This is in perfect

TABLE IV. Influence of variation of material parameters and of the discretization error on the calculated ground-state energies of electrons (E_{000}^{e}) and holes (E_{000}^{h}). The energy values (meV) refer to the VB edge of unstrained GaAs. The QD base width is 13.6 nm and the strain was calculated by the VFF model.

Set	Changed parameters	Unit	Values for GaAs	Values for InAs	E_{000}^{h}	E_{000}^{e}	ΔE
1	like no. 2, except				172.3	1269.4	1097
	voxel size		half lattice constant				
2	**reference set**				176.2	1274.5	1098
3	Like no. 2, except				170.8	1272.5	1102
	e_{14}	Cm^{-2}	$0.16 \rightarrow 0$	$0.045 \rightarrow 0$			
4	Like no. 3, except				237.3	1335.8	1099
	E_v'	meV		$-6747 \rightarrow -6670$			
5	Like no. 4, except				235.7	1345.7	1110
	E_p	eV	$28.0 \rightarrow 22.71$	$22.2 \rightarrow 20.2$			
6	Like no. 5, except				228.9	1343.5	1115
	a_c	meV	$-8013 \rightarrow -7170$				
	a_g	meV	$-8233 \rightarrow -8330$				
	b_v	meV	$-1824 \rightarrow -1600$				
	d_v	meV	$-5062 \rightarrow -4230$	$-3600 \rightarrow -3100$			
7	Like no. 6, except				223.4	1307.2	1084
	strain (ϵ_{ij})		reduced by 10 %				

agreement with the finding that CM and VFF applied to the QDs studied here produce effective electron confinement potentials differing by 20 meV.[34]

To facilitate the comparison with the results from Refs. 20 and 23 we note that these papers assumed band lineup B. Taking into account the different material parameters (set 7 in Table IV) and the discretization error, we find an extrapolated ground-state energy 22 meV below those from Refs. 20 and 23. We conclude that the differences between Fig. 4 and the quoted results are mainly due to different input values. Within 25 meV the results from Fig. 4 (using band lineup A) also agree with empirical pseudopotential calculations,[48] where the electron levels are slightly deeper confined than in our calculation. The reported separation between the electron $|100\rangle$ and $|010\rangle$ levels is 27 meV, i.e., three times larger than ours, however.

3. Hole levels (VFF)

The hole levels are in average 11 meV stronger localized than according to the CM calculation, otherwise no significant difference is observed. Repeating the above consideration we find agreement within 20 meV with the ground-state energies from Ref. 20, calculated by a four-band $\mathbf{k}\cdot\mathbf{p}$ model (a similar agreement between the four-band and eight-band models was observed in Ref. 24). We find different separations between excited hole levels, however.

The ground-state localization energy reported in Ref. 48 for $b=11.3$ nm is about 140 meV larger than according to Fig. 4. This points to a significantly different confinement potential used there, because we calculate the kinetic energy of the hole (electron) ground state to be only 64 meV (130 meV). In view of the acceptable agreement with our calculation regarding the electron levels such a difference seems counterintuitive.

VI. BOUND TWO-PARTICLE STATES

A. Exciton binding energies

Now the exciton ground-state binding energy as a function of the QD size for strain according to CM is calculated (VFF yields the same results). We use the Hartree approximation, i.e., a separable exciton wave function is assumed and the single electron and hole states, Ψ_e and Ψ_h, are determined self-consistently:

$$[H+V_e]\Psi_h=\tilde{E}_h\Psi_h, \quad [H+V_h]\Psi_e=\tilde{E}_e\Psi_e, \tag{14}$$

$$-e|\Psi_e|^2=\epsilon_0\nabla(\epsilon_s\nabla V_e), \quad e|\Psi_h|^2=\epsilon_0\nabla(\epsilon_s\nabla V_h), \tag{15}$$

where H is the empty dot Hamiltonian from Eq. (12). Equation 15 includes the effect of image charges like Eq. (10). If E_e and E_h denote the respective eigenvalues of H, then the exciton binding energy is

$$E_X=(E_e-E_h)-(\tilde{E}_e-\tilde{E}_h) -(\langle\Psi_h|V_e|\Psi_h\rangle-\langle\Psi_e|V_h|\Psi_e\rangle)/2. \tag{16}$$

TABLE V. Size (b) dependence of the electron ground-state Coulomb charging energy (E^e_{Coul}), the exciton ground-state binding energy (E_X), and of the polarization anisotropy index p for hypothetical direct recombination (direct) and excitonic recombination (exciton). p is defined by Eq. (22).

b (nm)	E^e_{Coul} (meV)	E_X (meV)	p (direct)	p (exciton)
10.2	24.8	26.1	0.056	0.052
13.6	24.3	21.7	0.098	0.089
17.0	20.7	15.6	0.18	0.15
20.4	17.8	11.0	0.26	0.16

The resulting energies E_X are listed in Table V. We find a monotonic dependence on the QD size, as expected. The nonmonotonicity reported in Ref. 25 is erroneous.

B. Electron ground-state Coulomb charging energy

The two-electron ground state is obtained in a similar manner, namely by solving

$$[H+V_e]\Psi_e=\tilde{E}_e\Psi_e, \quad -e|\Psi_e|^2=\epsilon_0\nabla(\epsilon_s\nabla V_e), \tag{17}$$

again including image charge effects. If E_e is the respective eigenvalue of H, the electron ground-state Coulomb charging energy is $E^{\mathrm{e}}_{\mathrm{Coul}}=\tilde{E}_e-E_e$. The resulting energies $E^{\mathrm{e}}_{\mathrm{Coul}}$ are also listed in Table V. Again we find an expected monotonic behavior.

VII. OPTICAL PROPERTIES

A detailed modeling of the optical properties of QDs and, moreover, self-organized QD ensembles is an intricate problem, even when restricted to the linear range. This is mainly due to two reasons:

(1) The population of an individual QD with charge carriers at sufficiently low temperatures is independent of that of others. No position independent Fermi level exists and rate equations with average level populations are incorrect. In general an ensemble of QDs has to be treated as a large set of microstates whose possible transitions are modeled by master equations.[57]

(2) The energy levels and particle wave functions in a QD depend on the population. Apart from spin effects, the Coulomb interaction alters the energy level structure in a nontrivial way. This actually requires to calculate true many-body states for all possible populations of the dot. One possibility to do so is to work out substantially simplified, fully analytical models (for excitons, see Refs. 58 and 59, for many-electron states see Refs. 60–64), another one is to perform self-consistent, mostly numerical calculations (Ref. 21 or this work).

The ansatz for arbitrary, realistic geometries, material and strain distributions we propose here is mostly designed for applications in the frame of QD laser research based on III-V compounds. For an ideal QD laser, homogeneous ensembles of QDs are desirable, with possibly few energy levels in the dots, which (at appropriate injection) support lasing mostly

or only on the biexciton ground state. Such dots must be sufficiently small so that confinement effects are dominant, electron levels are widely separated, excitons are weakly correlated,[58] and Coulomb interaction can be treated as a correction of the kinetic quantization effects.[65] Therefore we restrict ourselves to calculate the exciton and two-electron ground states within the Hartree approximation, where exchange and correlation interactions are discarded. Corrections for biexciton states are of the order of 2 meV.[66] The electron term scheme governs the main structure of the recombination spectra while the less widely separated hole levels contribute to the fine structure.

We model the linear absorption spectra of single QDs, which to a certain degree can be measured by photoluminescence excitation,[67] calorimetric absorption,[1] and transmission spectroscopy.[68] Within the dipole approximation the linear absorption coefficient of the QD is proportional to[27,53]

$$I_{ab}=\frac{\pi e^2\hbar^2}{\epsilon_0 m_0^2}\,\frac{2}{V}|\hat{e}\cdot\mathbf{p}_{ab}|^2=\frac{2\pi e^2}{\epsilon_0 V}\left|\hat{e}\left\langle a\left|\frac{\partial H}{\partial\mathbf{k}}\right|b\right\rangle\right|^2, \quad (18)$$

where $\hat{e}$ is the direction unit vector of the electric field of the linearly polarized incident light, V is the QD volume, H is the QD Hamiltonian from Eq. (12), $\mathbf{k}$ is the wave-number operator, $\mathbf{p}_{ab}$ is the momentum matrix element of the transition from state $|a\rangle$ into state $|b\rangle$, e is the electron charge, m_0 the free electron mass, and ϵ_0 the vacuum permittivity constant. Inserting the envelope functions into Eq. (18) is equivalent to considering the central cell part of $\mathbf{p}_{ab}$ only while neglecting the envelope part,[23,53] a commonly accepted measure. We note that Eq. (18) provides the full treatment of the structural, $\mathbf{k}$-, and strain dependence of $\mathbf{p}$, i.e., the information on the QD is not only stored in $|a\rangle$ and $|b\rangle$.

Since spin-orbit coupling is neglected, and due to the absence of magnetic fields, all energy levels in the QD are spin degenerate: If Ψ_1 according to Eq. (13) is an eigenvector to Eq. (12) then

$$\Psi_2=\begin{pmatrix}\mathbf{0}_4 & -\mathbf{1}_4\\ \mathbf{1}_4 & \mathbf{0}_4\end{pmatrix}\bar{\Psi}_1, \quad \langle\Psi_1|\Psi_2\rangle=0 \quad (19)$$

is also an eigenvector ($\mathbf{0}_4$ and $\mathbf{1}_4$ are the 4×4 zero and identity matrix, respectively, and $\bar{\Psi}_1$ is the complex conjugate of Ψ_1). This is not the Kramers symmetry and also true for $B\neq0$ (Kane parameter) in Table II. The momentum matrix elements for nonexcitonic transitions are obtained by incoherent averaging over the degenerate eigenspaces a and b, giving

$$|\hat{e}\cdot\mathbf{p}_{ab}|^2=\tfrac{1}{4}\left(|\hat{e}\cdot\mathbf{p}_{a_1b_1}|^2+|\hat{e}\cdot\mathbf{p}_{a_2b_1}|^2+|\hat{e}\cdot\mathbf{p}_{a_1b_2}|^2+|\hat{e}\cdot\mathbf{p}_{a_2b_2}|^2\right), \quad (20)$$

where $|a_1\rangle$ and $|a_2\rangle$ ($|b_1\rangle$ and $|b_2\rangle$) satisfy Eq. (19). On the level of simplification persued here, the exciton recombination is modeled the same way, just using self-consistent states $|a\rangle$ and $|b\rangle$ according to Eq. (14) instead. At self-consistency the eigenspaces a and b are not orthogonal any more since they belong to two Hamiltonians differing in their confinement potential parts. However, for I_{ab} this does not matter since $\partial H/\partial\mathbf{k}$ is not altered by changing electrostatic potentials. The oscillator strength obtained this way is a lower bound for the true excitonic oscillator strength, since the actual two-particle character of the exciton[69] was lost by making the ansatz of a separable exciton wave function. However, we expect correct modeling of the reduction of the optical anisotropy due to exciton formation.

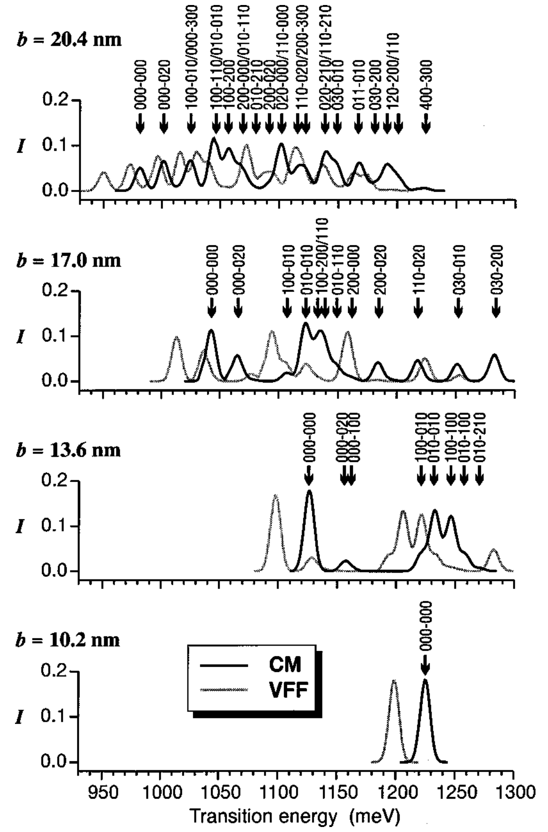

FIG. 9. Linear absorption spectra (electron-hole transitions, no excitonic correction) of InAs pyramid QDs of different sizes b for linearly [100] polarized light, calculated for strain distributions according to the CM (black) and VFF (gray) models. The arrows with ''quantum numbers'' refer to the black curve (CM) and indicate the strongest contributing transitions. The oscillator strength I is given by Eq. (21). The absorption lines are artificial Gaussians with 10 meV FWHM. The seemingly missing transitions for $b=20.4$ nm at energies above 1200 meV have not been calculated.

A. Electron-hole transitions

Figure 9 shows the linear absorption spectra for the interaction of QDs with $\hat{e}\|[100]$ polarized light, dependent on the dot size and the strain model. The dimensionless oscillator strength

$$I=\frac{2}{m_0E_p^{\mathrm{InAs}}}|\hat{e}\cdot\mathbf{p}_{ab}|^2 \quad (21)$$

refers to the bulk optical matrix parameter E_p of the QD material InAs and is the eight-band $\mathbf{k}\cdot\mathbf{p}$ analogon to the overlap integral $\langle\psi_a|\psi_b\rangle$ in the effective mass approximation. All corrections due to excitonic effects are neglected in this plot, and the transitions have been broadened artificially by Gaussians with 10 meV FWHM. Since at least for the

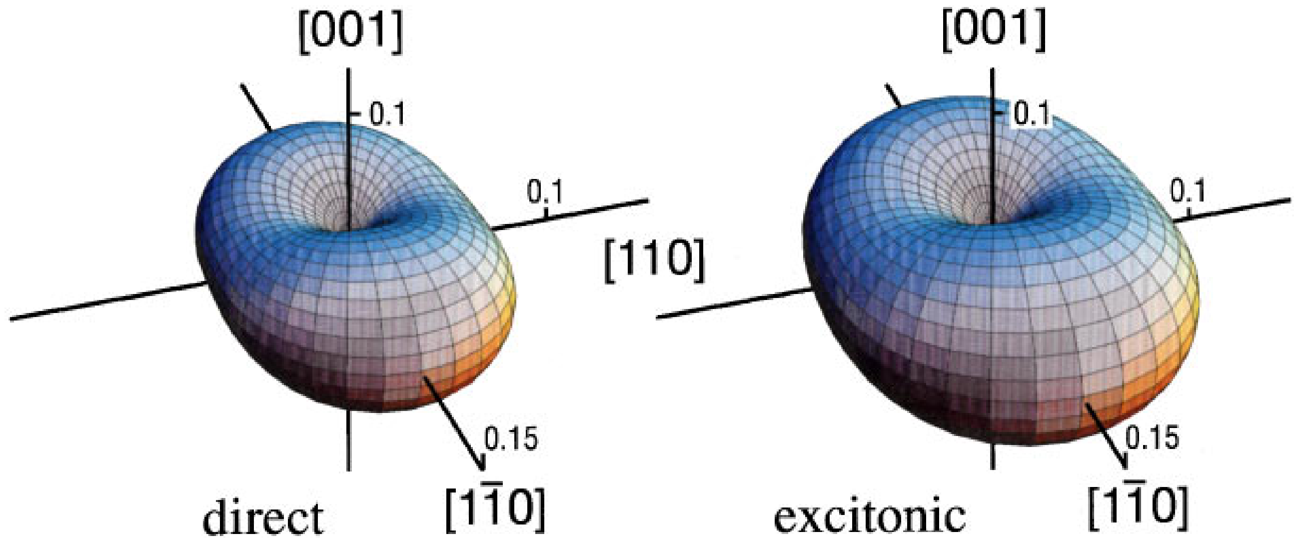

FIG. 10. (Color.) Oscillator strength I according to Eq. (21) as function of the direction of $\hat{e}$ (E field of light) for the electron-hole ground-state transition with and without excitonic (Coulomb) correction, calculated for $b=17.0$ nm using strain according to the CM model.

largest dots not all hole levels were calculated, the spectra for $b \geqslant 17.0$ nm are incomplete at high energies.

The spectra exhibit a large number of lines which mainly reflect the presence of several excited electron states. The assignment of the absorption lines to the respective transitions is also shown in Fig. 9. Some electron states yield a significant oscillator strength I with more than one hole state so that they contribute to more than one line. On the other hand, one line can be composed of several transitions, in particular when the inhomogeneous broadening becomes $\geqslant 20$ meV as it is in actual experiments. A significant decrease of I for the ground-states transition with increasing dot size is found. This is due to the piezoelectrically induced symmetry breaking of the hole ground state which reduces the overlap with the electron. For large dots the transition resembles a type II heterostructure.

B. Polarization anisotropy

Figure 10 shows the dependence of I on the direction of $\hat{e}$ according to Eq. (21) for the electron-hole ground-states transition for $b=17$ nm. There is a very strong anisotropy between the $[001]$ and $[xy0]$ polarization directions, and a weaker anisotropy between $[110]$ and $[1\bar{1}0]$. The latter reflects the C_{2v} symmetry of the single particle wave functions and is reduced by the Coulomb interaction between electron and hole. Therefore, excitonic transitions are expected to be less anisotropic than the inexisting recombination of ''free'' electrons and holes. The polarization anisotropy between the $[110]$ and $[1\bar{1}0]$ directions,

$$p=\frac{I_{[1\bar{1}0]}-I_{[110]}}{I_{[1\bar{1}0]}+I_{[110]}}, \tag{22}$$

of the ground-state transition is displayed in Table V for both cases, direct and excitonic recombination, and as function of the dot size b (strain according to CM). p increases with b and so does its reduction due to Coulomb interaction. Figure 11 shows p for all transitions in case of direct recombination, dependent on the dot size and the strain model. Both strain models yield the same trends. The interaction with $[001]$ polarized light is so much weaker for all transitions that the $[100]/[001]$ anisotropy index is almost constantly 1.

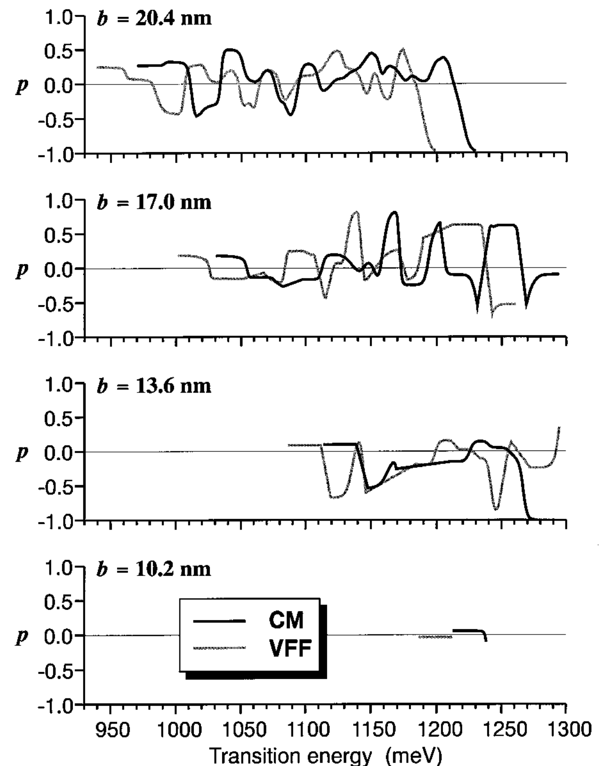

FIG. 11. Polarization anisotropy of the linear absorption (electron-hole transitions, no excitonic correction) between the $[110]$ and $[1\bar{1}0]$ directions for InAs pyramid QDs of different sizes b, calculated for strain distributions according to the CM (black) and VFF (gray) models. The seemingly missing transitions for $b=20.4$ nm at energies above 1200 meV have not been calculated.

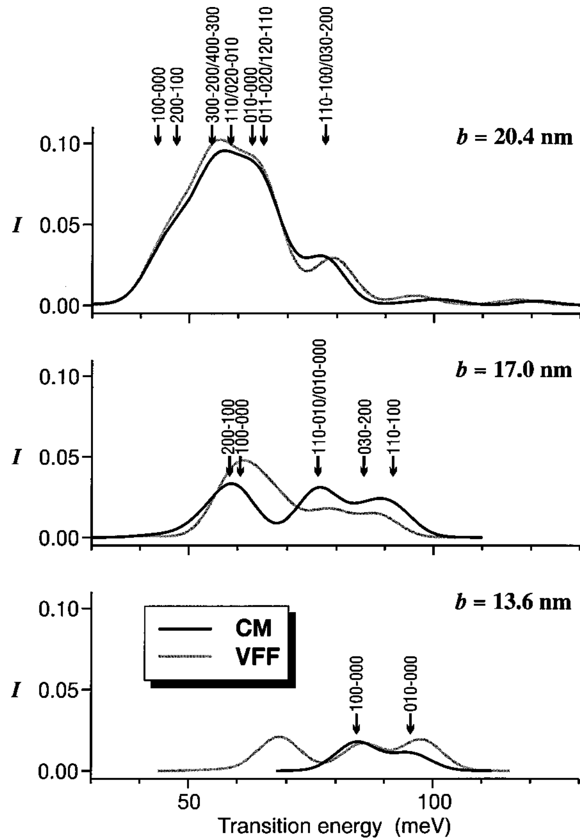

FIG. 12. Linear absorption spectra (electron-electron transitions) of InAs pyramid QDs of different sizes b for linearly [100] polarized light, calculated for strain distributions according to the CM (black) and VFF (gray) models. The arrows with ''quantum numbers'' refer to the black curve (CM) and indicate the strongest contributing transitions. The oscillator strength I is given by Eq. (21). The absorption lines are artificial Gaussians with 10 meV FWHM.

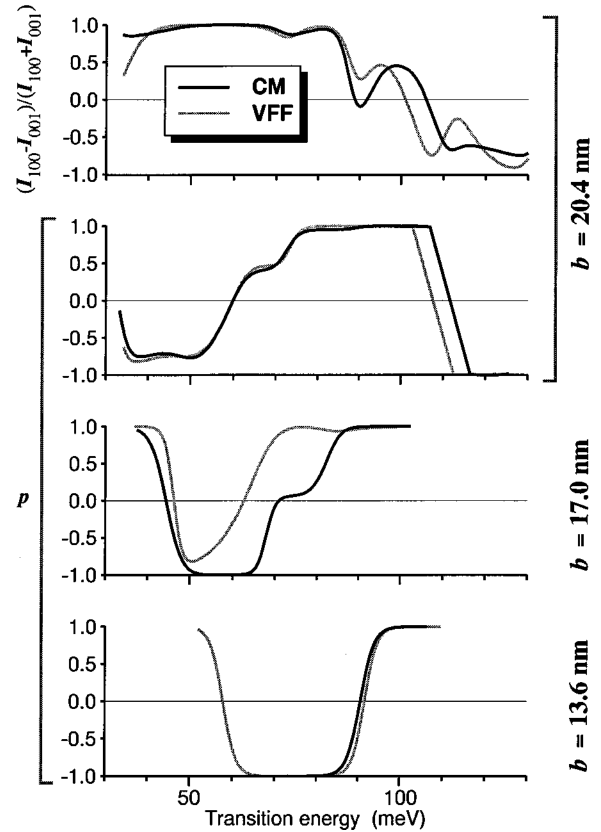

FIG. 13. Polarization anisotropy of the linear absorption (electron-electron transitions) between the [110]/[$1\bar{1}0$] and [100]/[001] directions, respectively, for different sizes b, calculated for strain distributions according to the CM (black) and VFF (gray) models. For $b=13.6$ nm and $b=17.0$ nm essentially $(I_{100}-I_{001})/(I_{100}+I_{001})=1$ over the entire energy range.

C. Electron-electron transitions

Transitions between electron levels are generally less intense and exhibit a stronger anisotropy than electron-hole transitions. Both are consequences of the strict dominance of the s-type Bloch parts in the electron wave functions (see Fig. 6).

The linear (far-infrared, FIR) absorption spectra for [100] polarization due to electron-electron transitions are shown in Fig. 12, dependent on the dot size and the strain model. Fig. 13 shows the corresponding polarization anisotropies between the [110] and [$1\bar{1}0$], and between the [100] and [001] directions. There is considerable interaction with light polarized in the substrate plane (001) which is a completely different situation from that in quantum wells. Thus infrared light detectors for perpendicular incidence of light are possible using QDs.

The assignment of the absorption lines to the transitions is also shown in Fig. 12. The majority of the excited electron states is involved in allowed FIR optical transitions. The maximum of the FIR absorption shifts slightly to lower energies and becomes significantly stronger as the dot size increases, due to an increasing number of allowed transitions.

VIII. CONCLUSIONS

We have systematically investigated the electronic and linear optical properties of capped quantum dots in the frame of the eight-band $\mathbf{k}\cdot\mathbf{p}$ model including piezoelectric effects. Numerical results for the model system of InAs quantum pyramids in GaAs (001) with {101} facets were presented. For four different dot sizes (base widths between 10 nm and 20 nm) we have calculated the bound electron and hole levels, the dipole transition energies, oscillator strengths, and polarization anisotropies, as well as the exciton ground-state binding energy and the electron ground-state Coulomb charging energy.

For the first time, a comparison of these properties for two different strain models was made, in order to examine the influence of the strain modeling on the resulting band structure and optical properties. We have worked out and compared the continuum elasticity theory and the valence force field model (Keating) in the linearized version (Kane). Continuum elasticity theory results are argued to come closer to reality. The two models yield slightly different strain distributions, which lead to slightly different level and transition energies, differences in the polarization and oscillator strengths of excited state transitions, and different spectra for electron-electron transitions. There is agreement, however, regarding the wave function shapes, the size dependence of the overall energy level structure, and the Coulomb charging and exciton binding energies.

The optical properties of such quantum dots are strongly influenced by the piezoelectric effect. We predict a pro-

nounced polarization anisotropy between the [110] and [1$\bar{1}$0] E-field directions and a decrease of the ground-state transition intensity with increasing dot size. The assignment of the transitions contributing to absorption lines is partly complex. Far-infrared absorption occurs mainly for light polarized in the substrate plane (001), in contrast to the case of quantum wells, and involves most of the present electron states.

ACKNOWLEDGMENTS

The authors would like to thank R. Heitz as well as V. Türck, C. M. A. Kapteyn, N. N. Ledentsov, A. Schliwa (TU Berlin), P. N. Brunkov (A. F. Ioffe Institute, St. Petersburg), and A. Zunger (NREL Golden, CO) for valuable discussions. This work was funded by Deutsche Forschungsgemeinschaft in the frame of Sfb 296.

[1] M. Grundmann, J. Christen, N. N. Ledentsov, J. Böhrer, D. Bimberg, S. S. Ruvimov, P. Werner, U. Richter, U. Gösele, J. Heydenreich, V. M. Ustinov, A. Yu. Egorov, A. E. Zhukov, P. S. Kop'ev, and Zh. I. Alferov, Phys. Rev. Lett. **74**, 4043 (1995); N. N. Ledentsov, M. Grundmann, N. Kirstaedter, J. Christen, R. Heitz, J. Böhrer, F. Heinrichsdorff, D. Bimberg, S. S. Ruvimov, P. Werner, U. Richter, U. Gösele, J. Heydenreich, V. M. Ustinov, A. Yu. Egorov, M. V. Maximov, P. S. Kop'ev, and Zh. I. Alferov, in *Proceedings of the 22nd International Conference on the Physics Semiconductors, Vancouver, Canada, 1994*, edited by D. J. Lockwood (World Scientific, Singapore, 1995), p. 1855.

[2] D. Bimberg, M. Grundmann, and N. N. Ledentsov, *Quantum Dot Heterostructures* (John Wiley & Sons, UK, 1998).

[3] M.-H. Mao, F. Heinrichsdorff, A. Krost, and D. Bimberg, Electron. Lett. **33**, 1641 (1997).

[4] D. Bimberg, N. Kirstaedter, N. N. Ledentsov, Zh. I. Alferov, P. S. Kop'ev, and V. M. Ustinov, IEEE J. Sel. Top. Quantum Electron. **3**, 196 (1997).

[5] S. Ruvimov, P. Werner, K. Scheerschmidt, U. Gosele, J. Heydenreich, U. Richter, N. N. Ledentsov, M. Grundmann, D. Bimberg, V. M. Ustinov, A. Yu. Egorov, P. S. Kop'ev, and Zh. I. Alferov, Phys. Rev. B **51**, 14 766 (1995).

[6] G. S. Solomon, M. C. Larson, and J. S. Harris, Appl. Phys. Lett. **69**, 1897 (1996).

[7] Y. Nabetani, T. Ishikawa, S. Noda, and A. Sasaki, J. Appl. Phys. **76**, 347 (1994).

[8] J. M. Moison, F. Houzay, F. Barthe, L. Leprince, E. André, and O. Vatel, Appl. Phys. Lett. **64**, 196 (1994).

[9] M. Tabuchi, S. Noda, and A. Sasaki, in *Science and Technology of Mesoscopic Structures*, edited by S. Namba, C. Hamaguchi, and T. Ando (Springer, Tokyo, 1992), p. 379.

[10] H. Lee, R. Lowe-Webb, W. Yang, and P. Sercel, Appl. Phys. Lett. **72**, 812 (1998).

[11] E. Dekel, D. Gershoni, E. Ehrenfreund, J. M. Garcia, and P. M. Petroff, in *Proceedings of the 24th International Conference on the Physics Semiconductors*, Jerusalem, Israel, 1998, edited by D. Gershoni (World Scientific, Singapore, 1998).

[12] L. Landin, M. S. Miller, M.-E. Pistol, C. E. Pryor, S. Jeppesen, B. Kowalski, and L. Samuelson (Ref. 11).

[13] Y. Shiraki, K. Ota, and N. Usami (Ref. 11).

[14] Y. Toda, K. Suzuki, and Y. Arakawa (Ref. 11).

[15] J.-Y. Marzin and G. Bastard, Solid State Commun. **92**, 437 (1994).

[16] M. Grundmann, O. Stier, and D. Bimberg, Phys. Rev. B **52**, 11 969 (1995).

[17] M. Fricke, A. Lorke, J. P. Kotthaus, G. Medeiros-Ribeiro, and P. M. Petroff, Europhys. Lett. **36**, 197 (1996).

[18] C. Guasch, C. M. Sotomayor Torres, N. N. Ledentsov, D. Bimberg, V. M. Ustinov, and P. S. Kop'ev, Superlattices Microstruct. **21**, 509 (1997).

[19] M. J. Steer, D. J. Mowbray, W. R. Tribe, M. S. Skolnick, M. D. Sturge, M. Hopkinson, A. G. Cullis, C. R. Whitehouse, and R. Murray, Phys. Rev. B **54**, 17 738 (1996); L. R. Wilson, D. J. Mowbray, M. S. Skolnick, M. Morifuji, M. J. Steer, I. A. Larkin, and M. Hopkinson, *ibid.* **57**, R2073 (1998); I. E. Itskevich, I. A. Trojan, S. G. Lyapin, D. Mowbray, M. S. Skolnick, M. Hopkinson, L. Eaves, P. C. Main, and M. Henini (Ref. 11).

[20] M. A. Cusack, P. R. Briddon, and M. Jaros, Phys. Rev. B **54**, R2300 (1996).

[21] L. R. C. Fonseca, J. L. Jimenez, and J. P. Leburton, and R. M. Martin, Phys. Rev. B **57**, 4017 (1998).

[22] H. Jiang and J. Singh, Physica E **2**, 614 (1998); **2**, 720 (1998); H. Jiang and J. Singh, Phys. Rev. B **56**, 4696 (1997); H. Jiang and J. Singh, Appl. Phys. Lett. **71**, 3239 (1997).

[23] H. Jiang and J. Singh, IEEE J. Quantum Electron. **34**, 1188 (1998).

[24] C. Pryor, Phys. Rev. B **57**, 7190 (1998).

[25] O. Stier, M. Grundmann, and D. Bimberg (Ref. 11).

[26] A. Zunger, MRS Bull. **23**, 35 (1998).

[27] P. Enders, A. Bärwolff, M. Woerner, and D. Suisky, Phys. Rev. B **51**, 16 695 (1995).

[28] A. S. Saada, *Elasticity: Theory and Applications* (Robert E. Krieger Publishing, Florida, 1989).

[29] M. J. P. Musgrave and J. A. Pople, Proc. R. Soc. London, Ser. A **268**, 474 (1962).

[30] P. N. Keating, Phys. Rev. **145**, 637 (1966).

[31] R. M. Martin, Phys. Rev. B **1**, 4005 (1970).

[32] E. O. Kane, Phys. Rev. B **31**, 7865 (1985).

[33] M. Podgorny, M. T. Czyzyk, A. Balzarotti, P. Letardi, N. Motta, A. Kisiel, and M. Zimnal-Starnawska, Solid State Commun. **55**, 413 (1985).

[34] C. Pryor, J. Kim, L.-W. Wang, A. Williamson, and A. Zunger, J. Appl. Phys. **83**, 2548 (1998).

[35] H. J. McSkimin and P. Andreatch, J. Appl. Phys. **35**, 3312 (1964); H. J. McSkimin and P. Andreatch, J. Appl. Phys. **38**, 2610 (1967).

[36] H. L. McMurry, A. W. Solbrig, Jr., J. K. Boyter, and C. Noble, J. Phys. Chem. Solids **28**, 2359 (1967); A. W. Solbrig, Jr., *ibid.* **32**, 1761 (1971).

[37] V. Türck, O. Stier, F. Heinrichsdorff, M. Grundmann, and D. Bimberg, Appl. Phys. Lett. **67**, 1712 (1995); V. Türck, O. Stier, F. Heinrichsdorff, M. Grundmann, and D. Bimberg, Phys. Rev. B **55**, 7733 (1997).

[38] L. V. Keldysh, Superlatt. Microstruct. **4**, 637 (1988).

[39] D. B. Tran Thoai, R. Zimmermann, M. Grundmann, and D. Bimberg, Phys. Rev. B **42**, 5906 (1990).

[40] M. Grundmann, O. Stier, and D. Bimberg, Phys. Rev. B **58**, 10 557 (1998).
[41] E. O. Kane, in *Handbook on Semiconductors Vol. I*, edited by W. Paul (North-Holland, Amsterdam, 1982).
[42] F. H. Pollak, Semicond. Semimet. **32**, 17 (1990).
[43] P. Enders, Phys. Status Solidi B **187**, 541 (1995).
[44] D. Gershoni, C. Henry, and G. Baraff, IEEE J. Quantum Electron. **29**, 2433 (1993).
[45] O. Stier and D. Bimberg, Phys. Rev. B **55**, 7726 (1997).
[46] Y. Zhang, Phys. Rev. B **49**, 14 352 (1994).
[47] M.-E. Pistol, M. Gerling, D. Hessman, and L. Samuelson, Phys. Rev. B **45**, 3628 (1992).
[48] J. Kim, L.-W. Wang, and A. Zunger, Phys. Rev. B **57**, R9408 (1998).
[49] *Properties of Lattice-Matched and Strained Indium Gallium Arsenide*, edited by P. Bhattacharya (INSPEC, London, 1993).
[50] C. G. Van de Walle, Phys. Rev. B **39**, 1871 (1989).
[51] *Landolt-Börnstein, Numerical Data and Functional Relationships in Science and Technology, New Series* (Springer, Berlin, 1982), Vol. III/17a.
[52] T. E. Ostromek, Phys. Rev. B **54**, 14 467 (1996).
[53] S. L. Chuang, *Physics of Optoelectronic Devices* (John Wiley & sons, New York, 1995).
[54] S. Adachi, *Physical Properties of III-V Semiconductor Compounds* (John Wiley & Sons, New York, 1992).
[55] *Properties of Gallium Arsenide*, 2nd ed. (INSPEC, London, 1990).
[56] H. Fu, L.-W. Wang, and A. Zunger, Phys. Rev. B **57**, 9971 (1998); H. Fu, L.-W. Wang, and A. Zunger, Appl. Phys. Lett. **71**, 3433 (1997).
[57] M. Grundmann and D. Bimberg, Phys. Rev. B **55**, 9740 (1997); M. Grundmann and D. Bimberg, Jpn. J. Appl. Phys. **36**, 4181 (1997).
[58] G. W. Bryant, Phys. Rev. B **37**, 8763 (1988).
[59] L. Jacak, J. Krasnyi, M. Korkusiński, and A. Wójs, Phys. Rev. B **57**, 9069 (1998).
[60] S. Tarucha, D. G. Austing, T. Honda, R. J. van der Hage, and L. P. Kouwenhoven, Phys. Rev. Lett. **77**, 3613 (1996).
[61] A. Wójs, P. Hawrylak, Phys. Rev. B **53**, 10 841 (1996).
[62] M. Koskinen, M. Manninen, and S. M. Reimann, Phys. Rev. Lett. **79**, 1389 (1997).
[63] E. Anisimovas and A. Matulis, J. Phys.: Condens. Matter **10**, 601 (1998).
[64] A. Matulis, J. O. Fjaerestad, and K. A. Chao, Phys. Scr. **T69**, 85 (1997).
[65] G. Medeiros-Ribeiro, F. G. Pikus, P. M. Petroff, and A. L. Efros, Phys. Rev. B **55**, 1568 (1997).
[66] Ph. Lelong and G. Bastard, in *Proceedings of the 23rd International Conference on Physics and Semiconductors* (Berlin, Germany, 1996), edited by M. Scheffler and R. Zimmermann (World Scientific, Singapore, 1996), p. 1377.
[67] R. Heitz, A. Kalburge, Q. Xie, M. Grundmann, P. Chen, A. Hoffmann, A. Madhukar, and D. Bimberg, Phys. Rev. B **57**, 9050 (1998); R. Heitz, M. Veit, N. N. Ledentsov, A. Hoffmann, D. Bimberg, V. M. Ustinov, P. S. Kop'ev, and Zh. I. Alferov, *ibid.* **56**, 10 435 (1997).
[68] R. J. Warburton, C. S. Dürr, K. Karrai, J. P. Kotthaus, G. Medeiros-Ribeiro, and P. M. Petroff, Phys. Rev. Lett. **79**, 5282 (1997).
[69] T. Takagahara, Phys. Rev. B **47**, 4569 (1993).